



PERSIANN Dynamic Infrared–Rain Rate (PDIR-Now): A Near-Real-Time, Quasi-Global Satellite Precipitation Dataset

PHU NGUYEN,^a MOHAMMED OMBADI,^a VESTA AFZALI GOROOH,^a ERIC J. SHEARER,^a MOJTABA SADEGHI,^a SOROOSH SOROOSHIAN,^a KUOLIN HSU,^a DAVID BOLVIN,^b AND MARTIN F. RALPH^c

^a Center for Hydrometeorology and Remote Sensing, Department of Civil and Environmental Engineering, University of California, Irvine, Irvine, California

^b Mesoscale Atmospheric Processes Laboratory, NASA GSFC, Greenbelt, Maryland

^c Center for Western Weather and Water Extremes, Scripps Institution of Oceanography, University of California, San Diego, La Jolla, California

(Manuscript received 22 July 2020, in final form 15 September 2020)

ABSTRACT: This study presents the Precipitation Estimation from Remotely Sensed Information Using Artificial Neural Networks–Dynamic Infrared Rain Rate (PDIR-Now) near-real-time precipitation dataset. This dataset provides hourly, quasi-global, infrared-based precipitation estimates at $0.04^\circ \times 0.04^\circ$ spatial resolution with a short latency (15–60 min). It is intended to supersede the PERSIANN–Cloud Classification System (PERSIANN-CCS) dataset previously produced as the near-real-time product of the PERSIANN family. We first provide a brief description of the algorithm’s fundamentals and the input data used for deriving precipitation estimates. Second, we provide an extensive evaluation of the PDIR-Now dataset over annual, monthly, daily, and subdaily scales. Last, the article presents information on the dissemination of the dataset through the Center for Hydrometeorology and Remote Sensing (CHRS) web-based interfaces. The evaluation, conducted over the period 2017–18, demonstrates the utility of PDIR-Now and its improvement over PERSIANN-CCS at all temporal scales. Specifically, PDIR-Now improves the estimation of rain/no-rain days as demonstrated by a critical success index (CSI) of 0.53 compared to 0.47 of PERSIANN-CCS. In addition, PDIR-Now improves the estimation of seasonal and diurnal cycles of precipitation as well as regional precipitation patterns erroneously estimated by PERSIANN-CCS. Finally, an evaluation is carried out to examine the performance of PDIR-Now in capturing two extreme events, Hurricane Harvey and a cluster of summer thunderstorms that occurred over the Netherlands, where it is shown that PDIR-Now adequately represents spatial precipitation patterns as well as subdaily precipitation rates with a correlation coefficient (CORR) of 0.64 for Hurricane Harvey and 0.76 for the Netherlands thunderstorms.

KEYWORDS: Rainfall; Precipitation; Remote sensing; Satellite observations; Neural networks

1. Introduction

Providing consistent and accurate precipitation measurements remains one of the most challenging tasks facing the weather and climate community. Rain gauge, radar, and satellite are the primary instruments for measuring precipitation. Rain gauge observations represent the most direct method for precipitation measurement and provide the longest historical records (Kidd and Levizzani 2011; Mahmoud et al. 2018); however, the variability of precipitation across all spatial and temporal scales cannot be resolved by conventional rain gauges. For instance, it has been shown that rainfall associated with small-scale convective storms vary by up to 14% over a 100-m distance (Goodrich et al. 1995). Radar instruments, which provide real-time precipitation measurements at

high spatiotemporal resolution, are attractive alternatives to rain gauges (Kitzmilller et al. 2013; Price et al. 2014). However, the high installation and maintenance costs along with the difficulties in accessibility over remote regions have limited the establishment of a global radar network (Habib et al. 2012; Westrick et al. 1999; Scofield and Kuligowski 2003). Satellite-based precipitation estimation promises to provide a remedy for the shortcomings of observing precipitation using radars and in situ rainfall gauges (Sun et al. 2018; Xie et al. 2007). Early studies that attempted to estimate rain rate from satellite multichannel visible (VIS) and infrared (IR) imagery dates back to the late 1970s (Griffith et al. 1978; Hsu et al. 1997). Today, four decades since the work of Griffith et al. (1978), estimation of precipitation from satellites has significantly advanced, and satellite-based estimates are frequently merged with in situ precipitation measurements to provide high-quality datasets (e.g., Huffman et al. 2007; Beck et al. 2017) for a range

Denotes content that is immediately available upon publication as open access.

Corresponding author: Phu Nguyen, ndphu@uci.edu

Publisher’s Note: This article was revised on 26 March 2021 to designate it as open access.

DOI: 10.1175/JHM-D-20-0177.1

© 2020 American Meteorological Society. For information regarding reuse of this content and general copyright information, consult the AMS Copyright Policy (www.ametsoc.org/PUBSReuseLicenses).

of hydrologic and hydroclimatic applications. Nonetheless, the ever-continuing search for an “optimum” method to accurately estimate precipitation from satellites, made evident by the dozens of datasets currently available to the community, stands as a testimony that the potential of satellites is yet to be fully realized.

The main difficulty in estimating precipitation from satellites lies in the trade-off between sampling temporal frequency and accuracy. On one hand, IR imagery data from sensors on board geostationary-Earth-orbiting (GEO) satellites are obtained almost every 5–30 min, but they only provide information on cloud-top characteristics (e.g., temperature, size, and the phase of cloud particles), an indirect proxy of surface precipitation rate (Grecu et al. 2004). On the other hand, passive microwave (PMW) sensors deployed on low-Earth-orbiting (LEO) satellites provide rich information on the vertical profile of the atmosphere and hydrometeors directly related to precipitation; however, their sampling is more sparse and less frequent compared to IR imagery (Behrangi et al. 2009; Marzano et al. 2004; Kidd and Levizzani 2011). Thus, IR-based precipitation estimation products have the advantage of providing higher spatiotemporal resolutions with a minimum latency that meet the requirements for many near-real-time applications (Arkin and Meisner 1987). More commonly, satellite-based algorithms take advantage of information from both IR and PMW sources (Behrangi et al. 2009; Joyce et al. 2004; Turk et al. 2000; Miller et al. 2001; Sorooshian et al. 2000; Hsu et al. 1997; Levizzani et al. 1996; Kummerow and Giglio 1995; Bellerby et al. 2000). Arguably, the most sophisticated example of such algorithms is the Climate Prediction Center morphing method (CMORPH) (Joyce et al. 2004), which relies on snapshot and propagated PMW as the primary source of precipitation, with IR estimates used over cold surface or when PMW is excessively propagated. Alternatively, several methods use IR data as the main input to derive an empirical relationship between cloud-top temperature and surface precipitation rate, and they incorporate PMW only for calibration purposes (Miller et al. 2001; Turk et al. 2003).

During the recent years, NOAA’s Advanced Baseline Imager (ABI) on board the latest generation of the Geostationary Operational Environment Satellite (GOES-R series) (Schmit et al. 2009, 2005; Gurka and Schmit 2004), the Advanced Himawari Imager (AHI) (Letu et al. 2020), on board *Himawari-8/9* (H8/9), and the Advanced Geostationary Radiation Imager (AGRI) on board *Fengyun-4A* (FY-4A) (Yang et al. 2017) have been launched into the geostationary (GEO) orbit. These sensors provide high temporal information with 10–15-min coverage and high spatial information with 0.5–2 km for AHI and ABI sensors and 0.5–4 km for AGRI measurements in 16 (14 for AGRI) spectral bands. The new generations of GEO sensors have opened new opportunities to improve the precipitation estimates with both high spatial and high temporal resolutions. With this promising progress in GEO sensor technologies along with the advancements in machine learning (ML) techniques, such as support vector machines, random forests, artificial neural network (ANN), deep learning, the new generation of precipitation retrieval algorithms must outperform the current operational products (Meyer et al. 2016; Kuligowski et al. 2016; Sadeghi et al. 2019; Upadhyaya et al. 2020). In recent years, many studies have been conducted to utilize the generation sensor information to

improve the current precipitation retrieval algorithms. For example, Kuligowski et al. (2016) proposed the Self-Calibrating Multivariate Precipitation Retrieval (SCaMPR) algorithm as an operational precipitation product over the CONUS based on GOES-R series information. This dataset serves Spinning Enhanced Visible and Infrared Imager (SEVIRI) on board *Meteosat-8* as inputs and passive microwave (PMW) precipitation rate estimates from the Climate Prediction Center (CPC) combined microwave (MWCMB) dataset (Joyce et al. 2004) for training. Although the developed retrieval algorithms using new generation of sensors provide higher spatial and temporal resolution over the contiguous United States (CONUS), their spatial coverage limits their capability for global implementation.

The present study introduces a new global near-real-time dataset based primarily on IR imagery referred to as the Precipitation Estimation from Remotely Sensed Information Using Artificial Neural Networks (PERSIANN) Dynamic Infrared Rain Rate (PDIR-Now). PDIR-Now is intended to supersede PERSIANN-Cloud Classification System (PERSIANN-CCS) (Hong et al. 2004), which has been the standard near-real-time precipitation dataset produced by the Center for Hydrometeorology and Remote Sensing (CHRS) at University of California, Irvine. PDIR-Now is based on the PDIR algorithm (Nguyen et al. 2020), which, like other IR-based algorithms, depends on empirically derived cloud-top temperature–precipitation rate (T_b – R) relationships. PDIR, however, corrects for the errors that frequently result from such an approach by calibrating the empirical relationships regionally based on monthly precipitation climatology (Nguyen et al. 2020). In addition, the PDIR algorithm incorporates several techniques to further reduce estimation errors and uncertainties. Because PDIR-Now depends primarily on IR data, its main advantage is providing near-global precipitation estimates at a short latency (15–60 min), hence the acronym “Now.” In addition, PDIR-Now leverages from IMERG PMW dataset for training, however, the PDIR algorithm was trained using the MWCMB dataset.

The remainder of this article is organized as follows. Section 2 briefly introduces input data used for PDIR-Now development as well as baseline datasets used for evaluation. Section 3 provides an overview of the PDIR algorithm and its components, and it highlights how PDIR-Now differs from its predecessors. Section 4 provides a comprehensive evaluation of PDIR-Now against distinct baseline precipitation datasets across a variety of spatial and temporal scales. Section 5 sums up the evaluation results, draws conclusions and outlines future directions.

2. Data

a. Input data

1) IR DATA

This dataset is provided by the Climate Prediction Center at the National Weather Service. It merges 11- μ m brightness temperature (T_b) data from all available geostationary satellites (*GMS-5*, *GOES-8*, *GOES-10*, *Meteosat-7*, and *Meteosat-5*) into a single half-hourly IR T_b field at the 4-km spatial resolution (Janowiak et al. 2001). This dataset is the main input used to produce PDIR-Now precipitation estimates.

2) IMERG MERGED PMW PRECIPITATION

The high-quality PMW is one of several fields available in the Integrated Multisatellite Retrievals for GPM (IMERG) dataset. It is based on intercalibrated PMW estimates and provides a global, half-hourly estimate at the $0.1^\circ \times 0.1^\circ$ spatial resolution (Huffman et al. 2018). Precipitation estimates from this dataset, along with IR data, are used to develop the (T_b - R) relationships in the calibration period (2014–16). It should be emphasized that the microwave data are only used for calibration, not a real-time input.

3) WORLDCLIM 2 PRECIPITATION

A monthly, high spatial resolution (1 km^2) precipitation dataset developed by Fick and Hijmans from spatially interpolated weather stations data (Fick and Hijmans 2017), this dataset provides precipitation data for the period 1970–2000 over global land areas. It is used here as precipitation climatology to adjust the T_b - R relationships over global land.

4) PERSIANN-CDR

PERSIANN-Climate Data Record (CDR) (Ashouri et al. 2015) belongs to the PERSIANN family of precipitation datasets (Nguyen et al. 2019). It provides daily precipitation for the period (1983–delayed present) over land and oceans at (60°S – 60°N); precipitation estimates from PERSIANN-CDR are bias-adjusted using GPCP V2.3 monthly $2.5^\circ \times 2.5^\circ$. Here, PERSIANN-CDR is used to complement the land-based WorldClim 2 dataset by providing precipitation climatology over oceans which is used to adjust the T_b - R relationships.

b. Evaluation data

1) NCEP STAGE IV

The National Centers for Environmental Prediction (NCEP) provides Stage IV precipitation data at hourly temporal resolution and a spatial resolution of 4 km. This dataset is a multisensor analysis that includes gauge and WSR-88D radar data among others (Lin and Mitchell 2005). Stage IV is frequently used to perform evaluations of precipitation data because of its high spatiotemporal resolution, multidecadal extent, and proven accuracy from manual quality control (Beck et al. 2019). In the present study, Stage IV (hereafter referred to as ST4) is used as a baseline over the contiguous United States (CONUS) against which the performance of PDIR-Now and PERSIANN-CCS is benchmarked.

2) IMERG FINAL RUN

IMERG is a half-hourly $0.1^\circ \times 0.1^\circ$ precipitation dataset that uses both PMW and IR data. The “Final Run,” hereafter referred to as IMERGF, incorporates further information from gauges to create a high-quality global precipitation data with approximately 3.5 months delay (Huffman et al. 2018). It is used as a baseline for the global evaluation of daily precipitation estimates from PERSIANN-CCS and PDIR-Now.

3) GPCP 1DD

The Global Precipitation Climatology Project (GPCP) 1DD (V1.3) product combines data from satellites and gauges to provide a $1^\circ \times 1^\circ$ daily precipitation dataset for the period 1996–present (Huffman et al. 2001). GPCP 1DD’s high spatiotemporal

resolution and integration of gauge readings make it a valuable dataset for short-duration evaluations of high-resolution precipitation products. Daily precipitation estimates from this dataset are accumulated to monthly scale, and they are used here as a baseline for the global evaluation of monthly precipitation estimates from PERSIANN-CCS and PDIR-Now.

1-h KNMI gauge-adjusted radar

The Royal Netherlands Meteorological Institute (KNMI) provides hourly 1-km radar precipitation data that are bias adjusted using the KNMI rain gauge networks. This dataset is used to evaluate the performance of PERSIANN-CCS and PDIR-Now in estimating precipitation during an extreme rainfall event that hit the Netherlands in June 2019 as it is the highest spatiotemporal resolution gridded radar–gauge product available over the Netherlands.

4) GSMAP-NOW

The Japanese Aerospace Exploration Agency (JAXA) produces a series of satellite-derived precipitation products under the Global Satellite Mapping of Precipitation (GSMaP). Among the GSMaP products, GSMaP-Now is the most comparable to PDIR-Now since it is a near-real-time product mainly based on IR data, making it a valuable comparison dataset for PDIR-Now at sub-daily time scales for extreme hydroclimate events. It is used to evaluate a series of summer thunderstorms over the Netherlands.

3. PDIR algorithm

In 1997, the PERSIANN algorithm (Hsu et al. 1997; Sorooshian et al. 2000) was developed to provide high-resolution quantitative precipitation estimation (QPE). As its namesake states, the original PERSIANN algorithm provides rainfall estimates by using artificial neural networks (ANNs). From the original framework of the PERSIANN algorithm, a 36+ years archive of global, daily rainfall product named PERSIANN-CDR was produced using the Global Precipitation Climatology Project (GPCP) V2.3 monthly rainfall dataset and CPC 4-km IR T_b data from the beginning of the satellite era (Ashouri et al. 2015).

Original PERSIANN’s 2-day latency, a consequence of the PMW readings used as input to PERSIANN, made it unusable for applications where near-real-time measurements are needed, like flood modeling. To overcome this issue, PERSIANN-CCS forewent the use of PMW data and utilized a system of trained cloud-type models with characteristic T_b - R relationships produced by self-organizing feature maps (SOFMs) to estimate rainfall at short latency periods. In addition to the short latency period, PERSIANN-CCS’s sole reliance on IR data made the product available in hyperspatial resolution of 0.04° and hourly temporal resolution. However, without PMW data, the accuracy of PERSIANN-CCS is starkly impaired from original PERSIANN’s performance, especially for extreme precipitation and precipitation in topographically complex regions, such as western CONUS.

To overcome some of the accuracy issues of PERSIANN-CCS and improve estimates of extreme and orographic precipitation, where short latency QPE is sorely needed for flood modeling applications, Nguyen et al. (2020) developed the PDIR algorithm based largely on the framework of PERSIANN-CCS. As such,

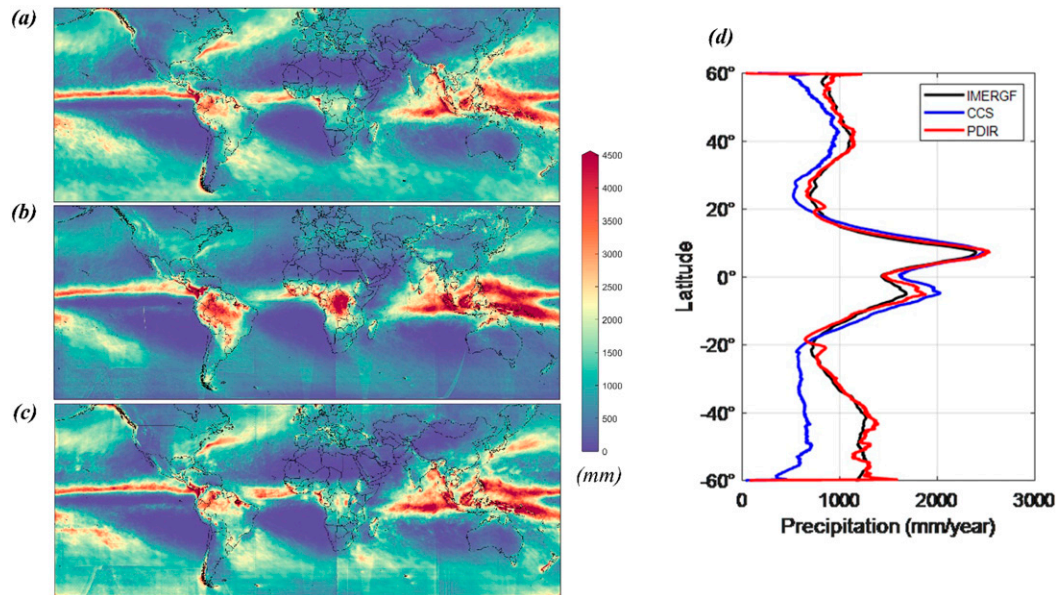


FIG. 1. Mean annual precipitation (mm) during the evaluation period (2017–18) for (a) IMERG-F (final release), (b) PERSIANN-CCS, and (c) PDIR-Now. (d) Zonal mean annual precipitation for the period (2017–18) for the three datasets: IMERG-F (black), PERSIANN-CCS (blue), and PDIR-Now (red).

PDIR is also a real-time, high-resolution precipitation product with short delay time (15 min–1 h) that uses a catalog of unique cloud types, created by training SOFMs with PMW data, to estimate rain rates based on the temperature, size, and texture features of the cloud patches at temperatures below 273 K. The defining feature of PDIR is the dynamical shifting of T_b – R curves using rainfall climatology data (spatiotemporal resolution of 0.04° and monthly) to adjust the curve's position. This approach is intended to adjust biases (i.e., to produce more precipitation in regions with wetter climatology and vice versa). As with PERSIANN-CCS, PDIR solely relies on near-real-time IR data from GEO satellites as input, allowing for precipitation estimates in as short as 15 min after their occurrences. For more information on the methodology of the PDIR algorithm, see [Nguyen et al. \(2020\)](#).

It should be noted that the PDIR-Now dataset presented in this article is based on the operational implementation of the PDIR algorithm which differs slightly from that originally described in [Nguyen et al. \(2020\)](#). Specifically, the current implementation employs a temperature threshold of 263 K for cloud top temperature as opposed to 273 K in [Nguyen et al. \(2020\)](#). This is because a higher temperature threshold improves the detection of warm rain events while simultaneously increasing the false alarm rate. In the earlier work of [Nguyen et al. \(2020\)](#), which examined the performance of the PDIR algorithm only over western United States, it was found that a threshold of 273 K achieves favorable results whereas a threshold of 263 K was found in the present study to be optimal for global implementation. Also, the precipitation dataset used to derive T_b – R curves in the present study is IMERG Merged PMW precipitation (see [section 2](#)) whereas the Combined Microwave precipitation dataset (MWCMB), produced by the CPC, was used in [Nguyen et al. \(2020\)](#). Moreover, the current implementation of the PDIR algorithm consists of an

additional bias adjustment step in which PDIR-Now rainfall estimates are corrected using probability cumulative density function (cdf) matching with IMERG Merged PMW precipitation. Last, PDIR-Now dataset is produced at a spatial resolution of 0.04° with a quasi-global coverage (60°S – 60°N).

4. Evaluation

This section evaluates the performance of PDIR-Now in capturing precipitation amounts and variability across several temporal scales. The evaluation commences at the coarsest temporal scale, annual, and then it is narrowed down to monthly, daily, and then subdaily scales. All analysis is conducted either during the entire evaluation period, 2017–18, or a part of it. Throughout the analysis, PDIR-Now will be compared with PERSIANN-CCS to highlight how much improvement has been attained using PDIR-Now. The baseline datasets against which PDIR-Now and PERSIANN-CCS are benchmarked varies according to geographical region and temporal scale of analysis.

a. Annual

Figures 1a–c show the mean annual precipitation averaged during the evaluation period (2017–18) for IMERG-F, PERSIANN-CCS, and PDIR-Now, respectively. Here, IMERG-F is used as a baseline since it combines data from multiple sources including IR, PMW, and gauges. Clearly, PERSIANN-CCS overestimates precipitation in the tropical regions of Africa, South America, and Asia. In addition, it underestimates bands of high precipitation in the northwestern Atlantic Ocean, northern Pacific Ocean along the coast of western Canada, and over the Southern Hemisphere oceans. This last observation is clearly shown in [Fig. 1d](#), which shows the average zonal annual precipitation. In particular, PERSIANN-CCS (blue line)

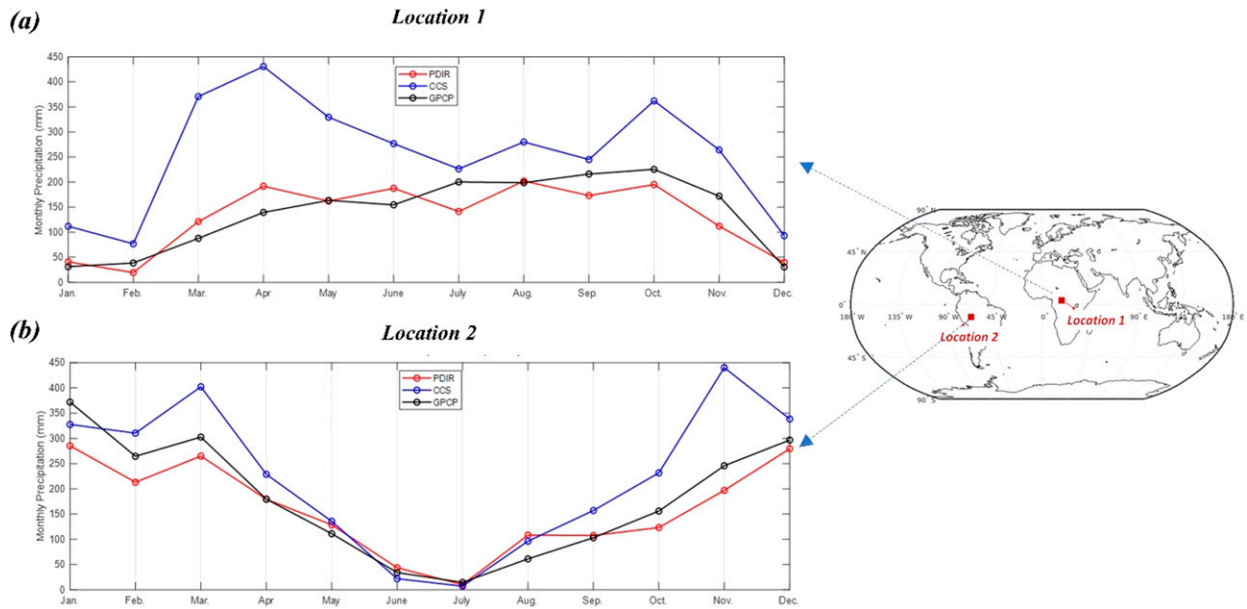


FIG. 2. Monthly precipitation time series for the year 2017. Black, blue, and red lines represent GPCP, PERSIANN-CCS, and PDIR-Now, respectively. (a) The $5^{\circ} \times 5^{\circ}$ region over Central Africa (location 1) bounded by the latitudes 1° – 6° N and longitudes 16° – 21° E. (b) The $5^{\circ} \times 5^{\circ}$ region over South America (location 2) bounded by the latitudes 13° – 8° S and longitudes 70° – 65° W.

deviates significantly from IMERGf over the latitudes (-60° , -20°) indicating considerable underestimation. On the other hand, PDIR-Now improves estimation significantly in terms of zonal precipitation as shown in Fig. 1d (red and black lines). In addition, it clearly captures bands of high precipitation previously underestimated by PERSIANN-CCS while reducing overestimation in tropical regions. Despite the improved performance of PDIR-Now, there are still apparent discrepancies between PDIR-Now and IMERGf. In particular, PDIR-Now overestimates bands of rainfall in western Pacific Ocean and scattered spots in central equatorial Africa. Overall, mean annual global precipitation from PDIR-Now is 1150 mm, and it is more consistent with IMERGf estimate of 1124 mm compared to 960 mm from PERSIANN-CCS.

b. Monthly

Here we examine the performance of PDIR-Now in capturing the seasonal cycle of precipitation, based on monthly precipitation, with GPCP 1DD precipitation being used as a baseline for evaluation. We carry out the analysis at two regions with distinct rainfall seasonal cycles. The first region (location 1) is a rectangular region bounded by the latitudes (1° – 6° N) and the longitudes (16° – 21° E). This region lies at the northwestern part of the Congo River basin with elevation in the range of 0–700 m above sea level. Due to its location in the tropics, rainfall is consistent throughout the year with slight peak during the months of August, September, and October; consequently, vegetation land cover mostly consists of evergreen broadleaf forest. Figure 2a shows the spatially averaged monthly precipitation for the year 2017. PDIR-Now (red line) closely follows the monthly GPCP precipitation (black line), capturing the slight peak in (August–October) period.

PERSIANN-CCS (blue line), on the other hand, overestimates rainfall amount throughout the year as well as showing an erroneous two-rainy-seasons cycle that differs from GPCP. Overall, the CORR and root-mean-square error (RMSE) of PDIR-Now are 0.83 and 43 mm, respectively, compared to 0.66 and 145 mm for PERSIANN-CCS. The second region (location 2) is in the humid Amazon rainforest bounded by the latitudes (13° – 8° S) and the longitudes (70° – 65° W), and it extends across Brazil, Bolivia, and Peru. Unlike location 1, this region exhibits a pronounced rainfall seasonal cycle with a very dry season during the months of June, July, and August. Figure 2b shows that both PERSIANN-CCS and PDIR-Now adequately capture the seasonal cycle of rainfall with CORR of 0.88 and 0.85, respectively; however, PDIR-Now improves estimation of rainfall amounts, most notably reducing the overestimation of PERSIANN-CCS during the months of October, November, and December. RMSE is reduced from 98 mm (PERSIANN-CCS) to 59 mm (PDIR-Now).

c. Daily

Despite the usefulness of the analysis presented in the previous two subsections for establishing the general validity of PDIR-Now, precipitation estimates at the daily and subdaily scales are more important from the standpoint of operational watershed hydrology and water resources management for applications such as flood forecasting. Furthermore, since PDIR-Now is an IR-based precipitation dataset, it is intended to be particularly advantageous in providing timely and adequate precipitation estimates when other datasets based on PMW and multisensor fusion are not available. With these considerations in mind, analysis of PDIR-Now at the daily and subdaily scales is carried out in this subsection and the following one.

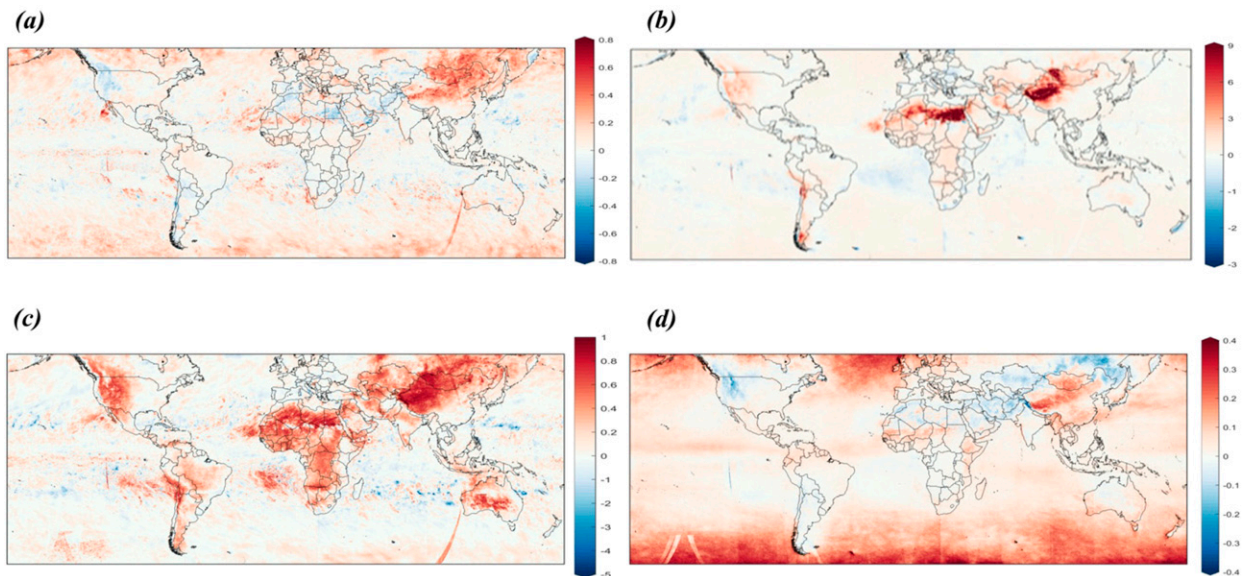


FIG. 3. Difference in performance metrics for daily rainfall during the evaluation period (2017–18). All metrics are computed against the baseline product IMERG. The maps show the difference between the performance metrics of PDIR-Now and PERSIANN-CCS; red color indicates that PDIR-Now has better performance with respect to PERSIANN-CCS. (a) Correlation, (b) relative bias, (c) relative RMSE (i.e., RMSE normalized by annual precipitation), and (d) CSI.

Figure 3 shows the difference in rainfall estimation statistics, namely CORR, bias, relative RMSE and CSI between PDIR-Now and PERSIANN-CCS benchmarked against IMERG. In other words, Fig. 3 shows the improvement obtained by PDIR-Now with respect to PERSIANN-CCS. Positive numbers (red colors in Fig. 3) indicate that PDIR-Now is more skillful compared to PERSIANN-CCS for a given metric meanwhile negative numbers (blue colors) indicate the opposite. Figure 3a shows the difference in CORR of daily precipitation. Apart from few regions in the Sahara Desert, Mediterranean Sea, and other scattered spots over oceans, PDIR-Now shows a better CORR compared to PERSIANN-CCS. While the average increase in CORR over the entire global domain is only marginal (0.52–0.57; see Table 1), significant regional improvement is present specifically over eastern Asia. Precisely, CORR in daily precipitation improves from 0.44 to 0.54 over the Asian continent (see Table 1). Similar patterns are observed in terms of bias in Fig. 3b with significant improvement over eastern Asia, central Africa, and Australia. Specifically, the biases are reduced from 2.07 to 0.28, from 1.38 to 0.06, and from 0.35 to 0.05 over the continents of Africa, Asia, and Australia, respectively. Figure 3c shows the improvement obtained in RMSE computed as the relative RMSE which is the RMSE difference ($\text{RMSE}_{\text{PERSIANN-CCS}} - \text{RMSE}_{\text{PDIR-Now}}$) normalized by $\text{RMSE}_{\text{PERSIANN-CCS}}$. It shows that PDIR-Now is superior to PERSIANN-CCS over most of the global land; specifically, RMSE in global land is reduced from 7 to 5.61 mm in PDIR-Now compared to PERSIANN-CCS. Figure 3d shows the difference in CSI which is a skill metric that summarizes the performance of the two algorithms in terms of their detection of rainfall events (rain/no rain). A threshold of 0.1 mm is used to distinguish between rainy and non-rainy days. It clearly shows that PDIR-Now is more skillful than PERSIANN-CCS in detecting rainfall events

and reducing false alarms over most regions, particularly over the Southern Hemisphere (60° – 40° S) oceans.

We now turn our analysis at the daily scale into regional scales of more unified precipitation regimes. Figure 4 shows the probability density functions (pdfs) of daily precipitation for each month spatially averaged over the northwestern United States region. The spatial domain considered here covers the entire states of Washington, Oregon, Idaho, Montana, Wyoming, and northern parts of California, Utah, and Colorado. We utilize ST4 dataset as a baseline for evaluation since it combines information from radar, satellite, and dense gauge network. Figure 4a shows the pdfs of daily precipitation during the year 2017 for values in the range of 1–6 mm. PDIR-Now pdfs are almost identical to those of ST4 for the rainy months of November, December, January, and February. While pdfs of PDIR-Now deviate from ST4 for some months, they provide mostly estimates better than that of PERSIANN-CCS. Similar conclusions, albeit less significant, can be drawn from Fig. 4b for high values of daily rainfall in the range of 6–20 mm. It should be noted that the improvement of PDIR-Now with respect to PERSIANN-CCS is expected to be particularly pronounced in this region due to its complex topography. Specifically, the motivation behind the development of PDIR-Now was to overcome the limitations of IR-based algorithm (e.g., PERSIANN-CCS) in estimating precipitation over complex terrain (Nguyen et al. 2020).

d. Subdaily

1) DIURNAL CYCLE

Here we examine the performance of PDIR-Now in capturing the diurnal cycle of precipitation at a regional scale,

TABLE 1. Summary statistics of comparison metrics for daily precipitation in the period (2017–18): correlation (CORR), root-mean-square error (RMSE), multiplicative bias (BIAS), probability of detection (POD), false alarm ratio (FAR), and critical success index (CSI). IMERGf is used as benchmark. Font style code: IMERGf (regular), PERSIANN-CCS (italic), PDIR-Now (bold). The asterisk (*) indicates the threshold for rain/no-rain = 0.1 mm.

Domain	Daily precipitation (mm)			CORR	BIAS	RMSE (mm)	POD*	FAR*	CSI*						
Global	3.08	2.63	3.15	0.52	0.57	0.08	0.02	7.82	7.80	0.54	0.63	0.21	0.24	0.47	0.53
Land	2.36	3.16	2.47	0.53	0.58	1.08	0.12	7.00	5.61	0.72	0.72	0.24	0.22	0.58	0.60
Ocean	3.36	2.44	3.41	0.51	0.56	-0.28	-0.02	8.13	8.62	0.47	0.59	0.20	0.24	0.42	0.50
Asia	2.11	2.86	2.15	0.44	0.54	1.38	0.06	6.92	5.18	0.72	0.69	0.28	0.24	0.56	0.57
North America	2.27	2.52	2.34	0.56	0.60	0.39	0.04	6.01	5.38	0.72	0.75	0.18	0.21	0.61	0.62
Europe	2.25	1.91	2.55	0.50	0.54	-0.09	0.13	5.61	6.08	0.70	0.81	0.15	0.22	0.62	0.66
Africa	1.89	3.47	2.05	0.57	0.59	2.07	0.28	7.11	4.86	0.72	0.67	0.31	0.24	0.55	0.57
South America	4.38	5.68	4.54	0.64	0.64	0.61	0.11	9.56	8.13	0.77	0.78	0.15	0.14	0.68	0.69
Oceania	5.71	3.84	6.89	0.52	0.57	-0.34	0.36	11.48	13.18	0.65	0.82	0.08	0.15	0.61	0.70
Australia	1.25	1.59	1.30	0.58	0.62	0.35	0.05	5.76	4.44	0.61	0.66	0.20	0.20	0.53	0.56
North Atlantic	3.39	1.71	3.25	0.51	0.56	-0.44	-0.04	8.23	8.76	0.51	0.65	0.18	0.24	0.46	0.54
North Pacific	3.38	2.40	3.38	0.47	0.55	-0.20	0.02	8.84	9.06	0.55	0.68	0.21	0.26	0.48	0.55
Mid-Atlantic	2.17	1.81	2.17	0.55	0.57	-0.07	-0.13	5.53	6.04	0.35	0.36	0.32	0.30	0.31	0.32
Mid-Pacific	3.96	3.93	4.00	0.66	0.67	-0.08	-0.06	8.73	9.54	0.45	0.49	0.17	0.18	0.42	0.45
Mid-Indian	3.64	3.58	4.00	0.70	0.70	-0.08	0.06	9.28	10.59	0.47	0.52	0.16	0.19	0.43	0.47
South Atlantic	3.06	1.54	3.07	0.39	0.46	-0.45	-0.00	7.64	7.79	0.49	0.69	0.24	0.31	0.42	0.53
South Indian	2.79	1.30	2.93	0.37	0.46	-0.55	0.05	6.95	7.23	0.46	0.69	0.20	0.26	0.42	0.55
South Pacific	3.56	1.89	3.58	0.40	0.47	-0.47	-0.01	8.72	8.81	0.47	0.67	0.19	0.25	0.42	0.55

specifically over the U.S. state of Kansas. Although the climate in Kansas varies considerably ranging from humid continental in the north to humid subtropical in the south, patterns of diurnal cycle are consistent throughout most of the state. Specifically, the state experiences severe thunderstorms during the rainy seasons of summer and spring. Such storms cause a

salient signature in the diurnal cycle of precipitation as they mostly occur around noon time. Figure 5 shows the diurnal cycle during each season of the year for PDIR-Now (red), PERSIANN-CCS (blue), and the baseline dataset ST4 (black). Of concern are the summer (JJA) and spring (MAM) seasons during which the region receives most of its annual precipitation.

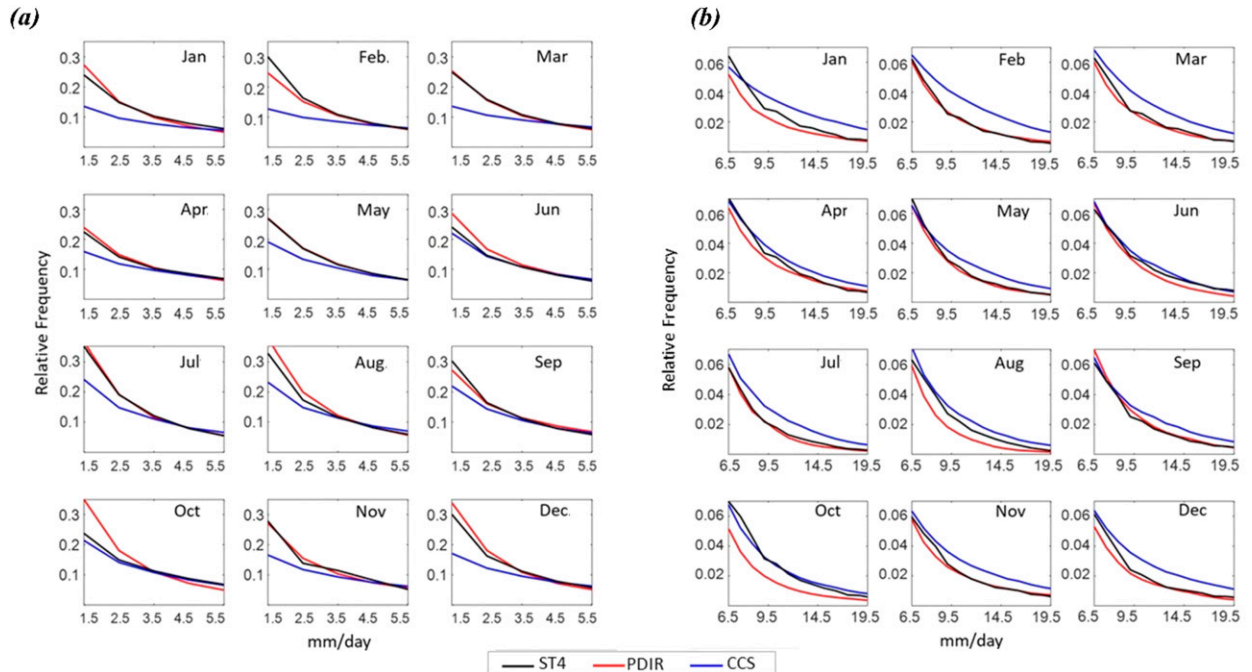


FIG. 4. Histograms of daily precipitation over the northwestern United States for the year 2017. Black, blue, and red lines represent ST4, PERSIANN-CCS, and PDIR-Now, respectively: (a) 1–6 and (b) 6–25 mm.

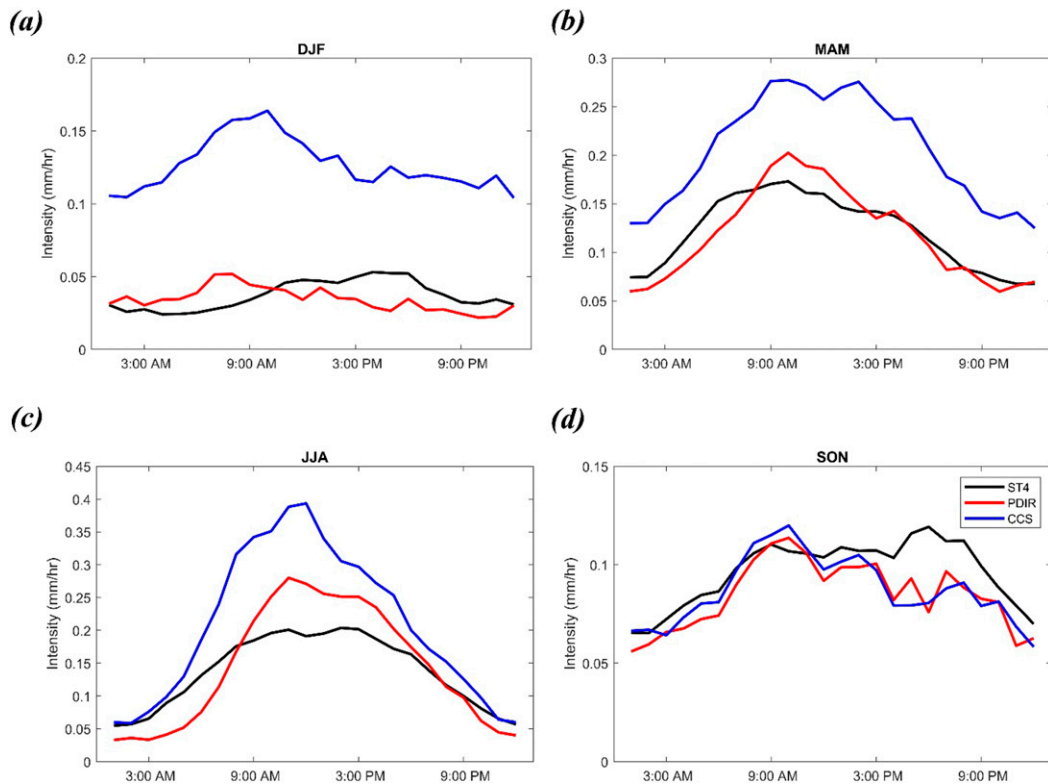


FIG. 5. Diurnal cycle of spatially averaged precipitation over Kansas for the period (2017–18). Black, blue, and red lines represent ST4, PERSIANN-CCS, and PDIR-Now, respectively. (a) DJF, (b) MAM, (c) JJA, and (d) SON.

Figures 5b and 5c show the pronounced diurnal cycle during these seasons. While both PERSIANN-CCS and PDIR-Now capture the diurnal cycle, which reaches its peak at noon time, PERSIANN-CCS overestimates the amount of rainfall in both seasons. PDIR-Now, however, estimates the amount of precipitation adequately during the spring season, and to a lesser extent in the summer season. During the winter months (DJF), Fig. 5a shows that PERSIANN-CCS substantially overestimates rainfall rates; on the contrary, PDIR-Now rainfall amount is quite consistent with ST4. However, it appears that the diurnal cycle in DJF as well as in SON are not well captured by PDIR-Now. This might be due to the low rain rates during both seasons, approximately 0.05 and 0.1 mm h^{-1} during DJF and SON respectively, as it is well recognized that satellite-based precipitation algorithms are generally less adept at estimating low rain rates. It is also worthwhile to mention that during both DJF and SON, the diurnal cycle is less pronounced; therefore, the estimates of ST4 are more susceptible to measurement noise.

2) EXTREME EVENTS

The performance of satellite-based precipitation datasets in capturing extreme rainfall events is of particular importance to be examined due to the important role that satellite observations can play in preparedness, risk management, and, in turn, mitigating the devastating impacts of such events. Here, we examine the performance of PDIR-Now in capturing precipitation during Hurricane Harvey, which resulted in unprecedented

rainfall accumulations of over 1.5 m that caused extensive flooding damage over the Houston metropolitan region, and an extreme rainfall event of thunderstorms that hit most of the Netherlands in June 2019, that resulted in damages, flooding, and injuries.

(i) Hurricane Harvey

To evaluate PDIR-Now's performance during Hurricane Harvey, we evaluate it against ST4 and compare its performance to PERSIANN-CCS over the states of Texas, Oklahoma, Kansas, Louisiana, Arkansas, and Alabama during the period of 24–30 August 2017. Figures 6a–c illustrate PDIR-Now's improved performance compared to PERSIANN-CCS at 6-h accumulations. Concretely, PDIR-Now's CORR of 0.64 , RMSE of 7.99 mm , and BIAS of -0.32 are all clear improvements over PERSIANN-CCS's CORR, RMSE, and BIAS values of 0.34 , 9.89 mm , and -0.53 , respectively. A quick look at the scatterplots between PDIR-Now and PERSIANN-CCS (Figs. 6d,e) show that while both products experience underestimation and overestimation, PDIR-Now better captures extreme precipitation, made evident by the band of points that straddle then dip slightly below the red line of perfect correlation. Indeed, PERSIANN-CCS's scatterplot hugs the x and y axes to its extrema with few points of extreme precipitation recorded near the line of perfect correlation, indicating systematic and extreme overestimation and underestimation with PERSIANN-CCS. PDIR-Now, on the other hand, suffers more from

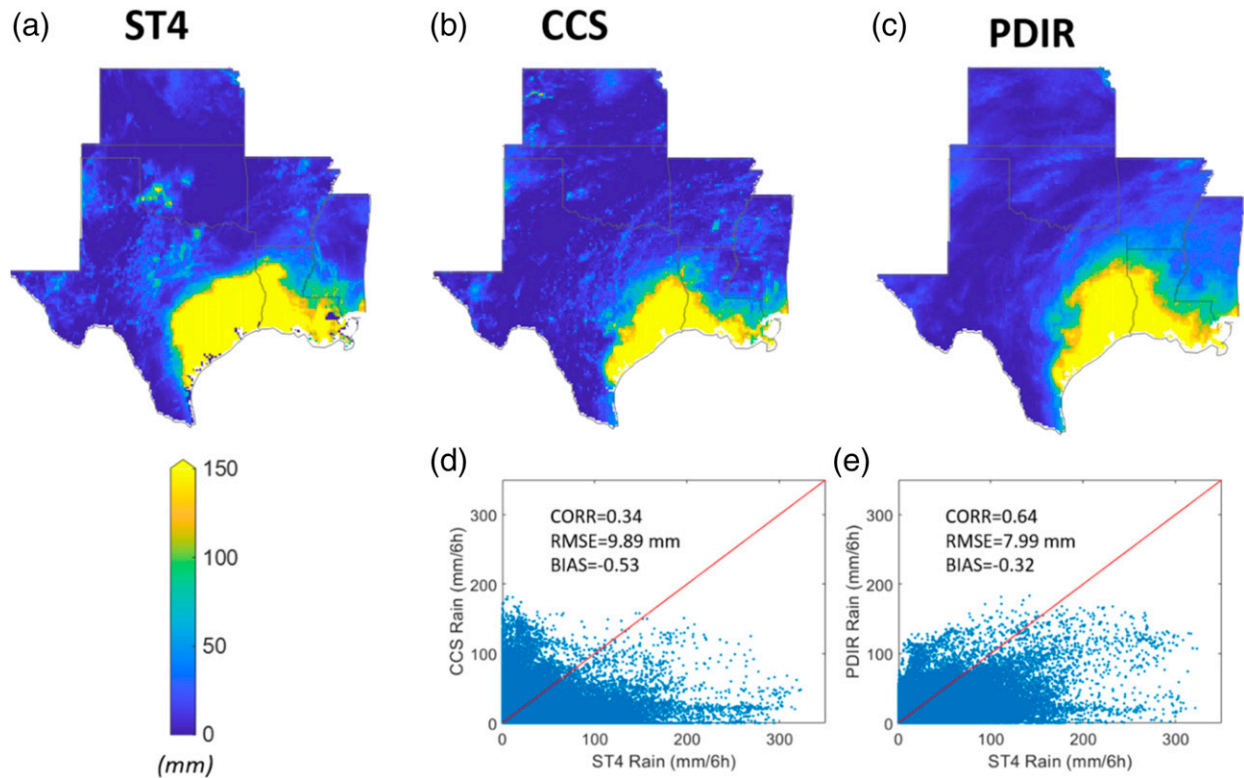


FIG. 6. Accumulated precipitation of Hurricane Harvey over Texas and the surrounding area for the period 24–30 Aug 2017 as estimated by (a) ST4, (b) PERSIANN-CCS, and (c) PDIR-Now. Scatterplots of 6-hourly precipitation from (d) PERSIANN-CCS vs ST4 and (e) PDIR-Now vs ST4 during the period 24–30 Aug 2017.

underestimation than overestimation, a testament to the unprecedented nature of precipitation during Hurricane Harvey, which has stumped other satellite QPE methodologies (Omranian et al. 2018). When we consider the spatial distribution of precipitation over the study period (Figs. 6a–c), there are few and subtle differences between PDIR-Now, PERSIANN-CCS, and ST4. Most notably, PDIR-Now's accumulation totals in northwest Louisiana/east Texas and in central Texas (Austin and San Antonio regions) better match those from ST4 than PERSIANN-CCS, though totals over the latter region are still underestimated by 50+ mm.

(ii) 2019 summer thunderstorms over the Netherlands

We use a high-quality dataset based on gauge-adjusted radar precipitation estimates provided by KNMI [see section 2b(4)] as a baseline for validation. Figure 7 shows the accumulated precipitation that resulted from the event during the period (3–6 June 2019) as estimated by gauge-adjusted radar, GSMaP-Now, PERSIANN-CCS, and PDIR-Now. Although PERSIANN-CCS captures the spatial variability of rainfall, it severely underestimates the amount of rainfall. GSMaP-Now, on the other hand, misses the pattern entirely, recording a blob of high precipitation from the center of the Netherlands to the southeast that does not appear in the evaluation radar–gauge dataset, while missing the bands of high precipitation over the

northwest region of the country. PDIR-Now, however, provides better estimates of rainfall amounts, especially over the western half of the Netherlands, though it appears to overestimate accumulated rainfall at the northeastern regions. These observations also manifest at the 3-hourly scale, shown by the scatterplots of 3-hourly rainfall during the entire event period for PDIR-Now, PERSIANN-CCS, and GSMaP-Now. Clearly, PERSIANN-CCS underestimates precipitation rates as evident by the cluster of points below the one-to-one line (red line). On the other hand, GSMaP-Now significantly overestimates rainfall, showcased by a positive bias, relatively large RMSE, and large patch of points above the red line of perfect correlation. Overall, CORR of 3-hourly rainfall are 0.76, 0.64, and 0.49 for PDIR-Now, PERSIANN-CCS, and GSMaP-Now, respectively.

5. Data dissemination and web-based interface

PDIR-Now dataset is available through two web-based interfaces operated by the Center for Hydrometeorology and Remote Sensing (CHRS) at the University of California, Irvine: the CHRS iRain interface (<https://irain.eng.uci.edu/>), a website that provides a user-friendly interface to visualize global precipitation dataset for the last 72 h, and the CHRS Data Portal (<https://chrsdata.eng.uci.edu/>), which is intended as an accessible interface for the download of PDIR-Now

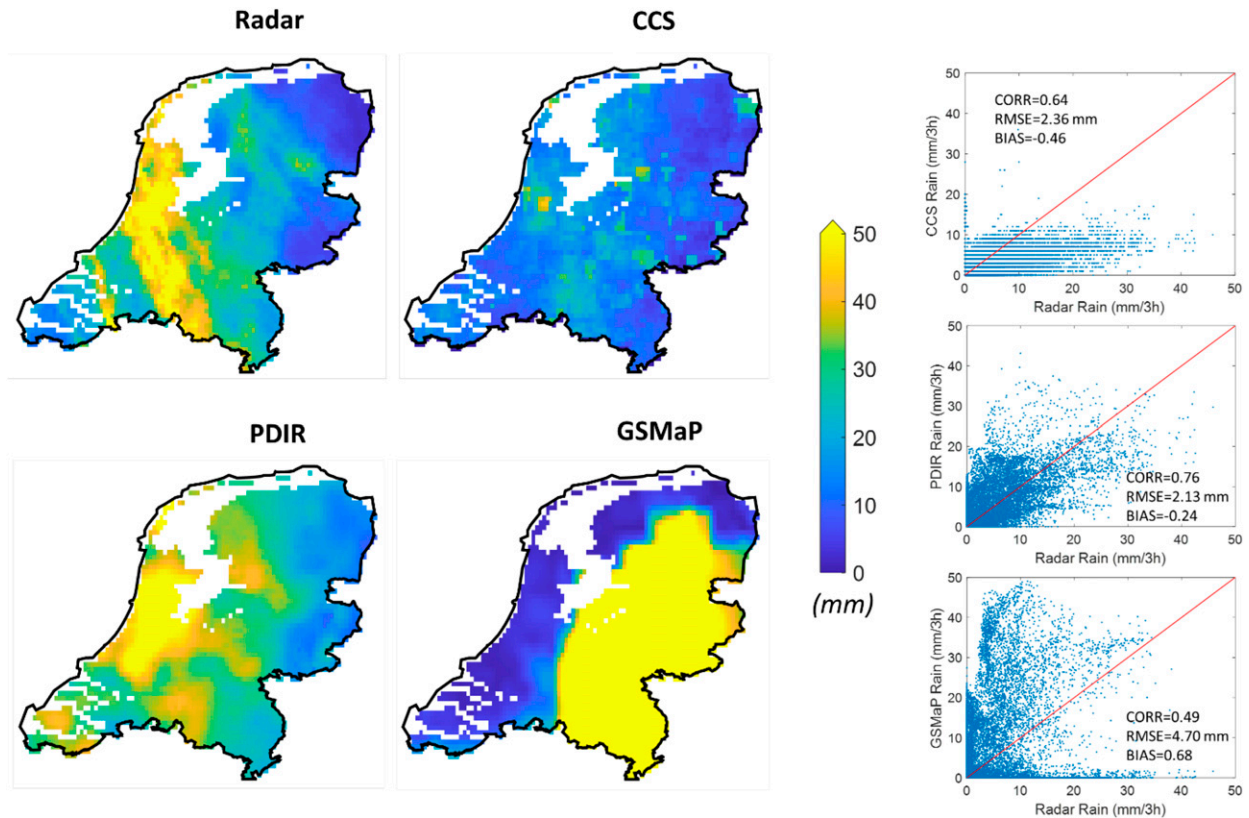


FIG. 7. Accumulated precipitation over the Netherlands for the period 3–6 Jun 2019 as estimated by KNMI gauge-adjusted radar, PERSIANN-CCS, PDIR-Now, and GSMap-Now. Scatterplots of 3-hourly precipitation from PERSIANN-CCS vs KNMI, PDIR-Now vs KNMI, and GSMap-Now vs KNMI during the period 3–6 Jun 2019.

dataset as well as other PERSIANN family datasets. The latter is described in detail in [Nguyen et al. \(2019\)](#). Here, we provide a brief description of the two interfaces.

a. CHRS data portal

The global PDIR-Now dataset is hosted for public distribution at CHRS's in-house data distribution web system, the CHRS Data Portal (chrsdata.eng.uci.edu; [Nguyen et al. 2019](#)). Currently, the span of the PDIR-Now dataset is from 1 January 2014 to the present, with a latency of 15–60 min after the time of occurrence. The CHRS Data Portal emphasizes ease of use by allowing users to query, process, compare, and analyze precipitation data onsite. In addition, it focuses on intuitive distribution by employing a simple data request system that allows users to aggregate and/or clip data over space and time prior to download. Data can be downloaded in binary, TIFF, NetCDF, and ArcGrid formats. Last, CHRS Data Portal's subscription tool allows users to receive rainfall information as soon as data are added to the archive.

b. CHRS iRain

The PDIR-Now dataset has replaced PERSIANN-CCS on the CHRS iRain web system (irain.eng.uci.edu) ([Fig. 8](#)). The iRain system is a web interface that allows users to visualize real-time global satellite precipitation observations from

PDIR-Now and track extreme precipitation events globally using the Connected-Object (CONNECT) algorithm ([Sellars et al. 2013](#)). The iRain interface consists of map layers which contain different political and hydrological borders that can be overlaid on the rainfall pattern and rain layers from different rain accumulation measurement tools such as radar, rain gauges, and crowd sourcing. Further information on iRain's tools and layers are provided in the subsections below.

1) MAP LAYERS

The iRain map layers tool ([Fig. 8a](#)) allows users to overlay polylines of political and hydrological divisions. For political divisions, users can query between overlaying country and political division (states, provinces, oblasts, etc.), while hydrologic divisions users can query include continental basins, major river basins, tributary basins, and watersheds.

2) RAIN LAYERS

The iRain rain layer tab ([Fig. 8b](#)) consists of four precipitation accumulation data products, including PDIR-Now, radar from Stage II, iRain's own crowdsourcing data, and rain gauges provided by MesoWest at the University of Utah. The combination of the data products found in iRain allows for a visualization and direct comparison of precipitation data from multiple sources at spatial scales from point to global. The rain

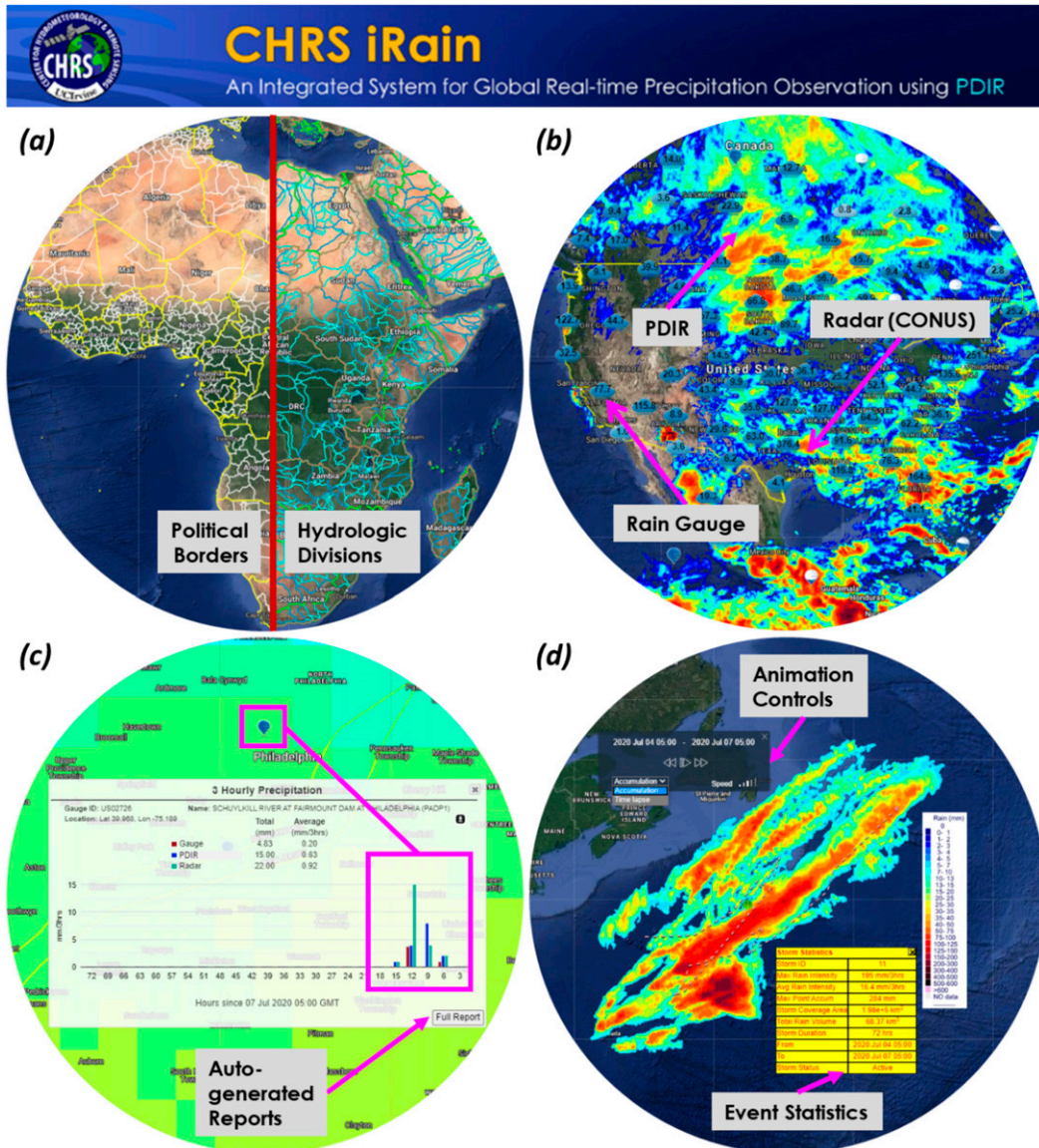


FIG. 8. CHRS iRain (<http://irain.eng.uci.edu>) and its various tools: (a) map layers, (b) rain layers, (c) rain query, and (d) extreme events.

total tab located under rain layers effects the rain layer tool, as it allows users to switch between the last 3 and 72 h of rain accumulation. Moreover, the 3-hourly rain animation tab displays an animation of 72-h rain accumulation.

3) SPATIAL QUERY

The spatial query tool (Fig. 8c) allows for users to select from nine different spatial extents. Users can query by the political and hydrological divisions from the map layers, create a user-customized rectangle or polygon, or query by point. The spatial query tool generates a graph of rainfall in that spatial extent over the last 3 days. Depending on the rain layers that are active, this plot can directly compare up to three data sources. Data and statistics autocalculated by this tool are

downloadable as an Excel spreadsheet for easy, deeper analysis. Selecting the full report option creates an autogenerated PDF of rainfall graphs, distributions, climatology, and geographic information such as distribution of aridity, land cover, and elevation. As with the autogenerated plots, this autogenerated PDF is downloadable directly off the web system.

4) EXTREME EVENTS

The iRain system allows users to track extreme precipitation events globally using the extreme events tab (Fig. 8d). The extreme event tool uses the CONNECT algorithm to produce four-dimensional (latitude and longitude spatial dimensions, temporal, and intensity) rainfall “objects” that allow for the tracking of large-scale precipitation event life cycles. With each

update of PDIR-Now data, CONNECT is automatically run on the system, and from it, the 50 largest-scale (based on intensity) precipitation events are stored for querying purposes. When the user interacts with the extreme events tool, the total accumulations of these 50 objects are displayed with a pointer that designates it with a number that corresponds to its rank in volume. Rainfall objects come with layers including centroids, which displays the total number of objects or storms; rain totals; tracking, which displays the polyline generated by each time-lapse spatial centroid; and the calculated statistics, which gives information on the storm such as storm intensity, accumulation, coverage area, total rain volume, duration, and status. Each storm is trackable through its time steps through either an accumulation or time-lapse animation. This animation's speed is customizable, and it also allows frame-by-frame navigation.

6. Concluding remarks

This article presented a new dataset, PDIR-Now, produced by the Center for Hydrometeorology and Remote Sensing (CHRS), which is intended to supersede PERSIANN-CCS. The dataset is evaluated across distinct temporal and spatial scales. It is shown that PDIR-Now is superior to PERSIANN-CCS in precipitation estimates at aggregate scales (i.e., continental and annual) as well as detection of seasonal and diurnal cycles of precipitation at regional scales. Furthermore, analysis of two extreme events, Hurricane Harvey and a cluster of summer thunderstorms over the Netherlands in August 2017 and June 2019, respectively, reveals that PDIR-Now significantly improves estimation of extreme events compared to PERSIANN-CCS, indicating better utility for applications where near-real-time readings of hydroclimate extremes are required.

The main advantage of PDIR-Now, compared to other near-real-time precipitation datasets, is its reliance on the high-frequency sampled IR imagery; consequently, the latency of PDIR-Now from the time of rainfall occurrence is very short (15–60 min). Additionally, PDIR-Now accounts for the errors and uncertainties that result from the use of IR imagery by adopting a variety of techniques most notable is the dynamic shifting of (T_b-R) curves using rainfall climatology. The short latency of PDIR-Now renders the dataset well suited for near-real-time hydrologic applications such as flood forecasting and developing flood inundation maps. Furthermore, the encouraging evaluation results in the present study indicate the potential of using the PDIR algorithm to reconstruct historical precipitation estimates at high spatiotemporal resolution. Preliminary investigations of such an avenue are underway, and their results will likely be reported in the foreseeable future.

Acknowledgments. This research was partially supported by the ICIWaRM of the U.S. Army Corps of Engineers, UNESCO's G-WADI program, Department of Energy (DOE Prime Award DE-IA0000018), California Energy Commission (CEC Award 300-15-005), University of California (4600010378 TO15 Am 22), and the National Oceanic and Atmospheric Administration (ST133017CQ0058) with Riverside Technology, Inc. The support

by NSF (Grant EAR-1928724) and NASA (Grant 80NSSC19K0726) to organize 12th International Precipitation Conference (IIPC12) and produce the IPC12 special collection of papers is gratefully acknowledged.

REFERENCES

- Arkin, P. A., and B. N. Meisner, 1987: The relationship between large-scale convective rainfall and cold cloud over the Western Hemisphere during 1982–84. *Mon. Wea. Rev.*, **115**, 51–74, [https://doi.org/10.1175/1520-0493\(1987\)115<0051:TRBLSC>2.0.CO;2](https://doi.org/10.1175/1520-0493(1987)115<0051:TRBLSC>2.0.CO;2).
- Ashouri, H., K.-L. Hsu, S. Sorooshian, D. K. Braithwaite, K. R. Knapp, L. D. Cecil, B. R. Nelson, and O. P. Prat, 2015: PERSIANN-CDR: Daily precipitation climate data record from multisatellite observations for hydrological and climate studies. *Bull. Amer. Meteor. Soc.*, **96**, 69–83, <https://doi.org/10.1175/BAMS-D-13-00068.1>.
- Beck, H. E., A. I. J. M. Van Dijk, V. Levizzani, J. Schellekens, D. Gonzalez Miralles, B. Martens, and A. De Roo, 2017: MSWEP: 3-hourly 0.25 global gridded precipitation (1979–2015) by merging gauge, satellite, and reanalysis data. *Hydrol. Earth Syst. Sci.*, **21**, 589–615, <https://doi.org/10.5194/hess-21-589-2017>.
- , and Coauthors, 2019: Daily evaluation of 26 precipitation datasets using Stage-IV gauge-radar data for the CONUS. *Hydrol. Earth Syst. Sci.*, **23**, 207–224, <https://doi.org/10.5194/hess-23-207-2019>.
- Behrangi, A., K. Hsu, B. Imam, S. Sorooshian, G. J. Huffman, and R. J. Kuligowski, 2009: PERSIANN-MSA: A precipitation estimation method from satellite-based multispectral analysis. *J. Hydrometeorol.*, **10**, 1414–1429, <https://doi.org/10.1175/2009JHM1139.1>.
- Bellerby, T., M. Todd, D. Kniveton, and C. Kidd, 2000: Rainfall estimation from a combination of TRMM precipitation radar and GOES multispectral satellite imagery through the use of an artificial neural network. *J. Appl. Meteor.*, **39**, 2115–2128, [https://doi.org/10.1175/1520-0450\(2001\)040<2115:REFACO>2.0.CO;2](https://doi.org/10.1175/1520-0450(2001)040<2115:REFACO>2.0.CO;2).
- Fick, S. E., and R. J. Hijmans, 2017: WorldClim 2: New 1-km spatial resolution climate surfaces for global land areas. *Int. J. Climatol.*, **37**, 4302–4315, <https://doi.org/10.1002/joc.5086>.
- Goodrich, D. C., J.-M. Faurès, D. A. Woolhiser, L. J. Lane, and S. Sorooshian, 1995: Measurement and analysis of small-scale convective storm rainfall variability. *J. Hydrol.*, **173**, 283–308, [https://doi.org/10.1016/0022-1694\(95\)02703-R](https://doi.org/10.1016/0022-1694(95)02703-R).
- Greco, M., W. S. Olson, and E. N. Anagnostou, 2004: Retrieval of precipitation profiles from multiresolution, multifrequency active and passive microwave observations. *J. Appl. Meteor.*, **43**, 562–575, [https://doi.org/10.1175/1520-0450\(2004\)043<0562:ROPPFM>2.0.CO;2](https://doi.org/10.1175/1520-0450(2004)043<0562:ROPPFM>2.0.CO;2).
- Griffith, C. G., W. L. Woodley, P. G. Grube, D. W. Martin, J. Stout, and D. N. Sikdar, 1978: Rain estimation from geosynchronous satellite imagery—Visible and infrared studies. *Mon. Wea. Rev.*, **106**, 1153–1171, [https://doi.org/10.1175/1520-0493\(1978\)106<1153:REFGSI>2.0.CO;2](https://doi.org/10.1175/1520-0493(1978)106<1153:REFGSI>2.0.CO;2).
- Gurka, J. J., and T. J. Schmit, 2004: Baseline instruments planned for the GOES-R series. *Proc. SPIE*, **5549**, 96–104, <https://doi.org/10.1117/12.555720>.
- Habib, E., A. T. Haile, Y. Tian, and R. J. Joyce, 2012: Evaluation of the high-resolution CMORPH satellite rainfall product using dense rain gauge observations and radar-based estimates. *J. Hydrometeorol.*, **13**, 1784–1798, <https://doi.org/10.1175/JHM-D-12-017.1>.
- Hong, Y., K.-L. Hsu, S. Sorooshian, and X. Gao, 2004: Precipitation estimation from remotely sensed imagery using an artificial

- neural network cloud classification system. *J. Appl. Meteor.*, **43**, 1834–1853, <https://doi.org/10.1175/JAM2173.1>.
- Hsu, K., X. Gao, S. Sorooshian, and H. V. Gupta, 1997: Precipitation estimation from remotely sensed information using artificial neural networks. *J. Appl. Meteor.*, **36**, 1176–1190, [https://doi.org/10.1175/1520-0450\(1997\)036<1176:PEFRST>2.0.CO;2](https://doi.org/10.1175/1520-0450(1997)036<1176:PEFRST>2.0.CO;2).
- Huffman, G. J., R. F. Adler, M. M. Morrissey, D. T. Bolvin, S. Curtis, R. Joyce, B. McGavock, and J. Susskind, 2001: Global precipitation at one-degree daily resolution from multisatellite observations. *J. Hydrometeorol.*, **2**, 36–50, [https://doi.org/10.1175/1525-7541\(2001\)002<0036:GPAODD>2.0.CO;2](https://doi.org/10.1175/1525-7541(2001)002<0036:GPAODD>2.0.CO;2).
- , and Coauthors, 2007: The TRMM multisatellite precipitation analysis (TMPA): Quasi-global, multiyear, combined-sensor precipitation estimates at fine scales. *J. Hydrometeorol.*, **8**, 38–55, <https://doi.org/10.1175/JHM560.1>.
- , and Coauthors, 2018: NASA Global Precipitation Measurement (GPM) Integrated Multi-satellite Retrievals for GPM (IMERG). Algorithm Theoretical Basis Doc., version 5.2, 35 pp., https://pmm.nasa.gov/sites/default/files/document_files/IMERG_ATBD_V5.2_0.pdf.
- Janowiak, J. E., R. J. Joyce, and Y. Yarosh, 2001: A real-time global half-hourly pixel-resolution infrared dataset and its applications. *Bull. Amer. Meteor. Soc.*, **82**, 205–218, [https://doi.org/10.1175/1520-0477\(2001\)082<0205:ARTGHH>2.3.CO;2](https://doi.org/10.1175/1520-0477(2001)082<0205:ARTGHH>2.3.CO;2).
- Joyce, R. J., J. E. Janowiak, P. A. Arkin, and P. Xie, 2004: CMORPH: A method that produces global precipitation estimates from passive microwave and infrared data at high spatial and temporal resolution. *J. Hydrometeorol.*, **5**, 487–503, [https://doi.org/10.1175/1525-7541\(2004\)005<0487:CAMTPG>2.0.CO;2](https://doi.org/10.1175/1525-7541(2004)005<0487:CAMTPG>2.0.CO;2).
- Kidd, C., and V. Levizzani, 2011: Status of satellite precipitation retrievals. *Hydrol. Earth Syst. Sci.*, **15**, 1109–1116, <https://doi.org/10.5194/hess-15-1109-2011>.
- Kitzmiller, D., D. Miller, R. Fulton, and F. Ding, 2013: Radar and multisensor precipitation estimation techniques in National Weather Service hydrologic operations. *J. Hydrol. Eng.*, **18**, 133–142, [https://doi.org/10.1061/\(ASCE\)JHE.1943-5584.0000523](https://doi.org/10.1061/(ASCE)JHE.1943-5584.0000523).
- Kuligowski, R. J., Y. Li, Y. Hao, and Y. Zhang, 2016: Improvements to the GOES-R rainfall rate algorithm. *J. Hydrometeorol.*, **17**, 1693–1704, <https://doi.org/10.1175/JHM-D-15-0186.1>.
- Kummerow, C., and L. Giglio, 1995: A method for combining passive microwave and infrared rainfall observations. *J. Atmos. Oceanic Technol.*, **12**, 33–45, [https://doi.org/10.1175/1520-0426\(1995\)012<0033:AMFCPM>2.0.CO;2](https://doi.org/10.1175/1520-0426(1995)012<0033:AMFCPM>2.0.CO;2).
- Letu, H., and Coauthors, 2020: High-resolution retrieval of cloud microphysical properties and surface solar radiation using Himawari-8/AHI next-generation geostationary satellite. *Remote Sens. Environ.*, **239**, 111583, <https://doi.org/10.1016/j.rse.2019.111583>.
- Levizzani, V., F. Porcu, F. S. Marzano, A. Mugnai, E. A. Smith, and F. Prodi, 1996: Investigating a SSM/I microwave algorithm to calibrate METEOSAT infrared instantaneous rainrate estimates. *Meteor. Appl.*, **3**, 5–17, <https://doi.org/10.1002/met.5060030102>.
- Lin, Y., and K. E. Mitchell, 2005: The NCEP Stage II/IV hourly precipitation analyses: Development and applications. *19th Conf. on Hydrology*, San Diego, CA, Amer. Meteor. Soc., 1.2, https://ams.confex.com/ams/Annual2005/techprogram/paper_83847.htm.
- Mahmoud, M. T., M. A. Al-Zahrani, and H. O. Sharif, 2018: Assessment of global precipitation measurement satellite products over Saudi Arabia. *J. Hydrol.*, **559**, 1–12, <https://doi.org/10.1016/j.jhydrol.2018.02.015>.
- Marzano, F. S., M. Palmacci, D. Cimini, G. Giuliani, and F. J. Turk, 2004: Multivariate statistical integration of satellite infrared and microwave radiometric measurements for rainfall retrieval at the geostationary scale. *IEEE Trans. Geosci. Remote Sens.*, **42**, 1018–1032, <https://doi.org/10.1109/TGRS.2003.820312>.
- Meyer, H., M. Kühnlein, T. Appelhans, and T. Nauss, 2016: Comparison of four machine learning algorithms for their applicability in satellite-based optical rainfall retrievals. *Atmos. Res.*, **169**, 424–433, <https://doi.org/10.1016/j.atmosres.2015.09.021>.
- Miller, S. W., P. A. Arkin, and R. Joyce, 2001: A combined microwave/infrared rain rate algorithm. *Int. J. Remote Sens.*, **22**, 3285–3307, <https://doi.org/10.1080/01431160152609155>.
- Nguyen, P., and Coauthors, 2019: The CHRS Data Portal, an easily accessible public repository for PERSIANN global satellite precipitation data. *Sci. Data*, **6**, 180296, <https://doi.org/10.1038/sdata.2018.296>.
- , E. J. Shearer, M. Ombadi, V. A. Goroooh, K. Hsu, S. Sorooshian, W. S. Logan, and M. Ralph, 2020: PERSIANN Dynamic Infrared-Rain rate model (PDIR) for high-resolution, real-time satellite precipitation estimation. *Bull. Amer. Meteor. Soc.*, **101**, E286–E302, <https://doi.org/10.1175/BAMS-D-19-0118.1>.
- Omranian, E., H. O. Sharif, and A. A. Tavakoly, 2018: How well can global precipitation measurement (GPM) capture hurricanes? Case study: Hurricane Harvey. *Remote Sens.*, **10**, 1150, <https://doi.org/10.3390/rs10071150>.
- Price, K., S. T. Purucker, S. R. Kraemer, J. E. Babendreier, and C. D. Knightes, 2014: Comparison of radar and gauge precipitation data in watershed models across varying spatial and temporal scales. *Hydrol. Processes*, **28**, 3505–3520, <https://doi.org/10.1002/hyp.9890>.
- Sadeghi, M., A. A. Asanjan, M. Faridzad, P. Nguyen, K. Hsu, S. Sorooshian, and D. Braithwaite, 2019: PERSIANN-CNN: Precipitation Estimation from Remotely Sensed Information Using Artificial Neural Networks–Convolutional Neural Networks. *J. Hydrometeorol.*, **20**, 2273–2289, <https://doi.org/10.1175/JHM-D-19-0110.1>.
- Schmit, T. J., M. M. Gunshor, W. P. Menzel, J. J. Gurka, J. Li, and A. S. Bachmeier, 2005: Introducing the next-generation advanced baseline imager on GOES-R. *Bull. Amer. Meteor. Soc.*, **86**, 1079–1096, <https://doi.org/10.1175/BAMS-86-8-1079>.
- , J. Li, S. A. Ackerman, and J. J. Gurka, 2009: High-spectral- and high-temporal-resolution infrared measurements from geostationary orbit. *J. Atmos. Oceanic Technol.*, **26**, 2273–2292, <https://doi.org/10.1175/2009JTECHA1248.1>.
- Scofield, R. A., and R. J. Kuligowski, 2003: Status and outlook of operational satellite precipitation algorithms for extreme-precipitation events. *Wea. Forecasting*, **18**, 1037–1051, [https://doi.org/10.1175/1520-0434\(2003\)018<1037:SAOOOS>2.0.CO;2](https://doi.org/10.1175/1520-0434(2003)018<1037:SAOOOS>2.0.CO;2).
- Sellars, S., P. Nguyen, W. Chu, X. Gao, K. Hsu, and S. Sorooshian, 2013: Computational Earth science: Big data transformed into insight. *Eos, Trans. Amer. Geophys. Union*, **94**, 277–278, <https://doi.org/10.1002/2013EO320001>.
- Sorooshian, S., K.-L. Hsu, X. Gao, H. V. Gupta, B. Imam, and D. Braithwaite, 2000: Evaluation of PERSIANN system satellite-based estimates of tropical rainfall. *Bull. Amer. Meteor. Soc.*, **81**, 2035–2046, [https://doi.org/10.1175/1520-0477\(2000\)081<2035:EOPSSSE>2.3.CO;2](https://doi.org/10.1175/1520-0477(2000)081<2035:EOPSSSE>2.3.CO;2).
- Sun, Q., C. Miao, Q. Duan, H. Ashouri, S. Sorooshian, and K. Hsu, 2018: A review of global precipitation data sets: Data sources, estimation, and intercomparisons. *Rev. Geophys.*, **56**, 79–107, <https://doi.org/10.1002/2017RG000574>.
- Turk, F. J., J. Hawkins, E. A. Smith, F. S. Marzano, A. Mugnai, and V. Levizzani, 2000: Combining SSM/I, TRMM and infrared geostationary satellite data in a near-realtime fashion for rapid

- precipitation updates: Advantages and limitations. *Proc. 2000 EUMETSAT Meteorological Satellite Data Users' Conf.*, Bologna, Italy, EUMP, 705–707.
- , E. E. Ebert, H.-J. Oh, B.-J. Sohn, V. Levizzani, E. A. Smith, and R. Ferraro, 2003: Validation of an operational global precipitation analysis at short time scales. Preprints, *12th Conf. on Satellite Meteorology and Oceanography*, Long Beach, CA, Amer. Meteor. Soc., CD-ROM, J1.2.
- Upadhyaya, S. A., P.-E. Kirstetter, J. J. Gourley, and R. J. Kuligowski, 2020: On the propagation of satellite precipitation estimation errors: From passive microwave to infrared estimates. *J. Hydrometeor.*, **21**, 1367–1381, <https://doi.org/10.1175/JHM-D-19-0293.1>.
- Westrick, K. J., C. F. Mass, and B. A. Colle, 1999: The limitations of the WSR-88D radar network for quantitative precipitation measurement over the coastal western United States. *Bull. Amer. Meteor. Soc.*, **80**, 2289–2298, [https://doi.org/10.1175/1520-0477\(1999\)080<2289:TLOTWR>2.0.CO;2](https://doi.org/10.1175/1520-0477(1999)080<2289:TLOTWR>2.0.CO;2).
- Xie, P., A. Yatagai, M. Chen, T. Hayasaka, Y. Fukushima, C. Liu, and S. Yang, 2007: A gauge-based analysis of daily precipitation over East Asia. *J. Hydrometeor.*, **8**, 607–626, <https://doi.org/10.1175/JHM583.1>.
- Yang, J., Z. Zhang, C. Wei, F. Lu, and Q. Guo, 2017: Introducing the new generation of Chinese geostationary weather satellites, Fengyun-4. *Bull. Amer. Meteor. Soc.*, **98**, 1637–1658, <https://doi.org/10.1175/BAMS-D-16-0065.1>.